# Accepted Manuscript

Flow Rate Impacts on Capillary Pressure and Interface Curvature of Connected and Disconnected Fluid Phases during Multiphase Flow in Sandstone

Anna L. Herring , Jill Middleton , Rick Walsh , Andrew Kingston , Adrian Sheppard

Please cite this article as: Anna L. Herring , Jill Middleton , Rick Walsh , Andrew Kingston , Adrian Sheppard , Flow Rate Impacts on Capillary Pressure and Interface Curvature of Connected and Disconnected Fluid Phases during Multiphase Flow in Sandstone, *Advances in Water Resources* (2017), doi: 10.1016/j.advwatres.2017.05.011

## Highlights

- We conduct quasi-static flow experiments, under three flow rates, in sandstone
- We link capillary pressure and image-based fluid-fluid interface curvatures
- We investigate capillary pressure-saturation relationships for different flow rates
- High capillary pressure (6.5 kPa) is successfully measured from image curvature
- Large air snap-off events are observed during drainage for all flow conditions

Flow Rate Impacts on Capillary Pressure and Interface Curvature of Connected and Disconnected Fluid Phases during Multiphase Flow in Sandstone

Anna L. Herring, Jill Middleton, Rick Walsh, Andrew Kingston, Adrian Sheppard

Anna Herring, PhD

Postdoctoral Research Associate

anna.herring@anu.edu.au<mailto:anna.herring@anu.edu.au>

Department of Applied Mathematics

Research School of Physics & Engineering

The Australian National University

Abstract
We investigate capillary pressure-saturation ($P_C$–S) relationships for drainage-imbibition experiments conducted with air (nonwetting phase) and brine (wetting phase) in Bentheimer sandstone cores. Three different flow rate conditions, ranging over three orders of magnitude, are investigated. X-ray micro-computed tomographic imaging is used to characterize the distribution and amount of fluids and their interfacial characteristics. Capillary pressure is measured via (1) bulk-phase pressure transducer measurements, and (2) image-based curvature measurements, calculated using a novel 3D curvature algorithm. We distinguish between connected (percolating) and disconnected air clusters: curvatures measured on the connected phase interfaces are used to validate the curvature algorithm and provide an indication of the equilibrium condition of the data; curvature and volume distributions of disconnected clusters provide insight to the snap-off processes occurring during drainage and imbibition under different flow rate conditions.

## 1.0 Introduction

Immiscible fluid displacement processes within solid porous media are ubiquitous in both engineered and natural subsurface systems; for example, during enhanced oil recovery operations when injected water or brine displaces oil, during $CO_2$ sequestration when injected $CO_2$ displaces reservoir brine in a saline storage reservoir, and during heavy precipitation events where water infiltration displaces air in vadose zone soils as the water table rises. Two critical parameters for describing these displacement processes, as well as the overall state of the fluid-fluid-porous media system, are (1) the difference in pressures between the two fluid phases (the capillary pressure, $P_C$) and (2) the fluid saturation (S) level within the porous media. It is common to report $P_C$ as a function of saturation, via what is termed the capillary pressure-saturation ($P_C$-S) curve, also known as the water retention curve.

The wetting properties of the solid matrix have a large impact on the $P_C$-S relationship of the fluids within the medium. In systems with two fluid phases, the solid surface generally exhibits a stronger affinity for one fluid relative to the other; the fluids are termed the "wetting" (W) and "nonwetting" (NW) phases, respectively; and the strength of the wetting properties of the solid can be measured by the contact angle ($\theta$) formed by the intersection of the fluid-fluid interface with the solid surface. $P_C$ is defined as the pressure difference between the wetting phase and nonwetting phase fluids across an interface:

$$P_C = P_{NW} - P_W \qquad \text{(egn. 1)}$$

$P_C$ is further linked to characteristics of the interface ($\sigma$, the interfacial tension between the two fluids; and $\kappa$, the curvature of the interface) via the Young-Laplace law:

$$P_C = 2\sigma\kappa \qquad \text{(egn. 2)}$$

As curvature is defined to be the inverse of the radius of curvature (R), for a simple cylindrical capillary tube, the curvature can be analytically linked to the tube radius (r) and solid surface contact angle ($\theta$):

$$\kappa = \frac{1}{R} = \frac{cos\theta}{r} \qquad \text{(egn. 3)}$$

However, for non-cylindrical, non-regular constrictions (as are found in natural porous media), eqn. 3 does not hold. In these cases, it is more useful to measure the *mean* curvature of the interface, which is the average of the two principle curvatures ($\kappa_1$ and $\kappa_2$); or alternatively, the average of the inverses of the two principle radii of curvature ($r_1$ and $r_2$):

$$\kappa = \frac{\kappa_1 + \kappa_2}{2} = \frac{1}{2}\left(\frac{1}{r_1} + \frac{1}{r_2}\right) \qquad \text{(egn. 4)}$$

From the definitions above, it is clear that in the Young-Laplace formulation $P_C$ is inherently a microscopic measurement, valid across stable interfaces. However, conceptually and in experimental applications, eqn. 1 is commonly applied on length scales applicable to core studies (e.g. Selker et al., 1999), and also during dynamic processes where interfaces are moving as exemplified by the measurement of Haines jumps (Haines, 1927) during dynamic flow processes (e.g. Berg et al., 2013).

Applying the macroscopic conceptualization given in eqn. 1, for a strongly water-wet system, a significant (positive) $P_C$ may be required to force nonwetting phase (such as oil or gas) into the pore spaces of the porous solid, this is termed the "entry pressure" of the system. Positive $P_C$ can be accomplished by increasing the pressure of the nonwetting phase (such as during a forced nonwetting phase injection), or by decreasing the pressure of the wetting phase (such as occurs when groundwater undergoes evapotranspiration by plants).

Saturation refers to the volume fraction of the pore space which is occupied by a given fluid phase, and is often presented in terms of the wetting phase saturation ($S_W$), although in some cases it is more convenient to describe the system in terms of the non-wetting phase saturation ($S_{NW}$). The two fluid saturation levels are related by eqn. 2:

$$S_{NW} + S_W = 1$$

(egn. 2)

The interdependence between the macroscopic $P_C$ and saturation values for a given system as described by the $P_C$-S relationship is both constitutive (i.e. a function of the porous media and the fluid phases present in the system) and hysteretic; the measurement and prediction of this relationship for various systems has been the subject of intensive research for several decades (e.g. Bear, 1972).

Most experimental studies measure the relationship between Pc and S by using tensiometers or pressure transducers to measure the fluid pressures, and mass-balance approaches or imaging methods to measure fluid saturation levels (Armstrong et al., 2012; Bear, 1972; Culligan et al., 2006; Herring et al., 2016a, 2015, 2014; Hou et al., 2012; Raeesi et al., 2014; Wildenschild et al., 2005). Often, the saturation values are averaged over the domain of the system, and the bulk measured pressure values are assumed to represent the pressure of all of a given fluid phase present within the system; and so an experimental domain is represented by a single macroscopic $P_C$ value (as defined in eqn. 1) and single saturation value (the validity of this simplification, as well as the translation between macroscale measurements and microscale interfacial features, is a topic of great debate; for example, see Hassanizadeh and Gray (1993)). For wetting phase within a very strongly wetting system, it is often assumed that a singular pressure measurement is representative of the pressure state of all the wetting fluid; in a strongly wetting system, wetting phase is connected via thin films and throughout the smallest throats and crevices of the medium (Morrow, 1990), so that changes in wetting phase pressure may be transmitted throughout the domain. However, for nonwetting phase, the assumption that measured pressure is representative of all nonwetting fluid cannot be considered to be accurate, because during flow, nonwetting fluid becomes disconnected and isolated within pore bodies of the solid matrix, and so pressure changes which occur in the bulk nonwetting phase are not transmitted to the isolated nonwetting clusters. Thus, pressure measurements of the nonwetting fluid phase are only accurate for nonwetting fluid pressure which is connected to the measurement device.

Several researchers have highlighted the role that disconnected fluid phases have in determining crucial constitutive measures; including impacts to fluid trapping amounts, $P_C$-S curves, and relative permeability relationships. Some researchers have incorporated the impact of disconnected phases in mathematical models by distinguishing between connected (sometimes called "percolating") and disconnected ("non-percolating") fluid phases (e.g. Besserer and Hilfer, 2000; Fischer et al., 1997; Hilfer, 2006, 1998; Hilfer and Doster, 2010; Youssef et al., 2010). Other studies have focused on the relationships between disconnected cluster characteristics and residual trapping (Armstrong et al., 2014; Hilfer et al., 2015); and on the impact that disconnected cluster mobilization has to relative permeability (Avraam and Payatakes, 1995; Rücker et al., 2015).

Although the importance of including disconnected fluid phases for flow and transport applications is known, direct measurement of cluster characteristics within opaque three-dimensional (3D) porous medium samples has previously been limited by experimental capabilities. Recently, image analysis techniques have progressed so that interfacial features can be identified and quantified with a high degree of accuracy, even at very small scales; this has allowed for measurement of fluid-fluid interfacial curvatures within 3D porous media systems. Armstrong et al. (2012) used the Young-Laplace equation (eqn. 2) to demonstrate that 3D curvatures could be measured from x-ray computed tomographic (x-ray CT) images and correlated with transducer-based $P_C$ up to approximately 300 Pa for oil-brine interfaces in glass bead packs; following this, Li et al. (n.d.) provided reanalysis of the data of Armstrong et al. (2012) and presented an updated method for image processing and curvature estimation which resulted in an improved fit between image-based curvatures and transducer-based pressure values. The ability to measure curvature from 3D tomographic images has provided opportunities to investigate the $P_C$ of individual ganglia during mobilization processes (Armstrong et al., 2014), and under reservoir conditions (Andrew et al., 2015, 2014). As of yet, the maximum $P_C$ which has been measured from 3D x-ray CT images is on the order of 2 kPa in the study of Andrew et al. (2015), equivalent in that study to a mean curvature of approximately 0.03 $\mu m^{-1}$ or 0.11 $voxel^{-1}$, representing a radius of curvature of 32 $\mu m$ or 9 voxels (Andrew et al., 2015).

Another unresolved issue with respect to experimental measurements of $P_C$ is the question of how to determine when "true" equilibrium has been established. Traditionally, Pc-S relationships were measured by executing a step change in the boundary pressure values and monitoring the resultant saturation change over time; due to the long timeframe required to reach stable saturation at each pressure step, a complete pressure saturation curve could require 10-40 days to acquire (Bear, 1972). While this method is still utilized, and improvements have been made to allow complete curves to be collected in shorter timeframes (Raeesi et al., 2014), an alternative $P_C$-S measurement method has been utilized in recent studies (including the present study) which uses a pump to effect a change in the saturation level of the sample; pressure values are then monitored and equilibrium is assumed when bulk phase pressure values have stabilized (e.g. Culligan et al., 2006; Plug and Bruining, 2007; Porter et al., 2010). The time-dependency of equilibration for experimental studies, and the related question of whether bulk-phase measured pressure values do accurately represent the stabilization of fluid interfaces within a porous media, have recently become topics of interest due to the improved quality of time-resolved data (Gray et al., 2015; Schlüter et al., n.d.). Gray et al. (2015) suggest that equilibrium may require significantly longer timescales than would be indicated by bulk-phase pressure measurements; but that equilibrium can be evaluated by whether the curvature of the micro-scale interfaces is reflected by the bulk (macroscale) phase pressure.

We utilize 3D x-ray CT imaging, combined with a novel curvature measurement algorithm (implemented in Mango, the in-house MPI-parallel 3D image analysis software (Sheppard et al., 2004)) to measure the $P_C$ across wetting-nonwetting phase (brine-air) interfaces within Bentheimer sandstone rock cores, and compare these pressure values with bulk-phase pressure measurements. The experiments aim to push the limits of spatial and temporal resolution of laboratory-based x-ray CT for the calculation of curvature within real rocks. Three sets of quasi-static drainage and imbibition experiments were conducted and analyzed, representing three different flow rate conditions (18, 286, and 3000 µl/hr; corresponding to capillary number values as reported in Table 1). Transducer-based $P_C$ values ranging up to approximately 40 kPa. We use precision image analysis to combine the curvature measurements of individual NW phase clusters (including two types of clusters: those which are connected to the bulk phase (i.e. those which percolate through the media, spanning to the top of the core), and those which are disconnected) with cluster volume. With this experimental data, we aim to investigate several questions related to $P_C$ measurement:

- Under what conditions is it possible to relate *macroscopic* transducer-based $P_C$ measurements to *microscopic* 3D image-based curvature measurements for two-phase fluid flows in sandstone?
- How does $P_C$ (as measured by interface curvature) manifest for connected and disconnected nonwetting phase (air) clusters?
- What is the impact of flow rate on connected and disconnected phase $P_C$ at equilibrium (as measured by interface curvature) for these quasi-static displacement experiments?

## 2.0 Materials and Methods

### 2.1 Core holder assembly

We utilized a modified version of the experimental set-up reported by Herring et al. (2016). Bentheimer sandstone cores, 4.5 mm diameter and 10 mm long, were installed within a titanium core holder which was manufactured in-house at the Australian National University (ANU). The wetting fluid for these experiments was degassed 1.0 M potassium-iodide (KI) brine, and the nonwetting fluid was ambient air. The bentheimer samples used in this study were strongly water-wet with a porosity (measured from x-ray CT data volumes) of 24.6%; more detailed mineralogical and petrophysical characteristics are reported elsewhere (Peksa et al., 2016, 2015). To achieve water-wet boundary conditions, two layers of semi-permeable membrane (pore size of 1.2 µm; General Electric Company, Fairfield CT, United States) were wrapped around the core longitudinally; two additional circular layers were placed below the core and compressed onto the lower axial face of the core via a viton o-ring. The layers of membrane around the core provided lateral water-wet boundary conditions and reduced preferential wall-flow of air, and those below the core prevented air breakthrough through the core and allowed for drainage to higher $P_C$ than could be achieved otherwise. The core holder was connected to the syringe pump (Harvard Apparatus, Holliston MA, United States) and pressure transmitter (Keller America, Inc., Newport News, VA, United States) by polyether ether ketone (PEEK) flow lines. A small, flexible air-tight reservoir made of thinly stretched paraffin wax was placed at the top outlet of the core holder, this prevented evaporation while maintaining a nonwetting phase (air) reservoir above the core at ambient pressure conditions.

## 2.2 Control of flow processes and data acquisition

The syringe pump and pressure transmitter were each connected to a laptop housing an in-house developed LabVIEW program, which (1) continuously recorded pressure and temperature via the pressure transmitter, (2) controlled the flowrate, volume, direction, and timing of pumping via the syringe pump, and (3) communicated via TCP socket connection with QRUMBA, the in-house image acquisition software which controls all x-ray CT imaging parameters. Three flow rate conditions were investigated: 18, 268, and 3000 µl/hr. For a given experiment, the flow rate condition was applied in both drainage and imbibition; capillary number values for both processes are reported in Table 1. For flow experiments, the core was first saturated under vacuum (recorded brine pressures indicated pressure of ≤-60 kPa relative to ambient conditions) to achieve relatively high brine saturation; in these experiments, the vacuum saturation process was successful for two experiments (the 18 and 3000 µl/hr experiments achieved a brine saturation of ≥94%), but only moderately successful for the third experiment (the 268 µl/hr experiment started with a brine saturation of 75%). Then the LabVIEW program was initiated, and the brine-saturated scan acquired. When the scan was complete, brine was drained from the sample at the desired flow rate until the air entry pressure (as previously determined during practice experiments) was achieved; pumping was then halted and the system was allowed to equilibrate for 5, 15, or 25 minutes (for 18, 268, and 3000 µl/hr flow rates, respectively), after which another scan commenced. Equilibration times were based on bulk phase pressure response (measured by transducer during practice experiments) at target $P_C$ ranges ($P_C$ of 0 kPa to approx. 10 kPa). Transducer response at very low brine pressures (i.e. transient pressure drops below approx.. -10 kPa) indicate that equilibration is not fully achieved within this time frame for very high $P_C$ conditions.  After this point, the LabVIEW program alternated stepwise pumping periods (wherein a fraction of a pore-volume was pumped), and subsequent equilibration and scan acquisitions (Figure 1) until the endpoint drainage pressure was reached (indicated by transient brine pressure ≤ -25, -30, and -50 kPa relative to starting pressure for 18, 268, and 3000 µl/hr flow rates, respectively), at which point a final drainage scan was acquired. Then, the stepwise pump-equilibration-scan acquisition cycle repeats for imbibition. The volume of brine pumped between each scan was determined by user input and was a fraction of a pore volume; the exact value was changed for different experiments to accommodate the overall time frame for each experiment. The total volume imbibed was always greater than one pore volume. In this way, the pumping-scanning process was automated, and several scans were collected throughout drainage and imbibition processes with no user interference or manipulation. Each double helical trajectory x-ray CT scan required approximately 80-90 minutes acquisition time (depending on the vertical pitch of the data collected, for each experiment nearly the entire vertical span of the rock was imaged); full drainage-imbibition experiments were completed in approximately 40 hours.

## 2.3 Transducer-based capillary pressure measurement

To determine the wetting phase (brine) pressure value representative for each scan from the transducer data, the continuously measured brine pressure was averaged over the time period of the scan; due to the physical location of the transducer (at the base of the x-ray CT hutch, approx. 0.6 - 0.85 m below the sample depending on stage height), the averaged pressure values were also be corrected for hydrostatic pressure (i.e. see initial pressure readings at time of approx. 0-2 hrs in Figure 1). Connected nonwetting phase (air) pressure was assumed to be equivalent to ambient pressure throughout the course of the experiment, as the air reservoir at the top of the core holder was maintained at ambient pressure. $P_C$ values were calculated following Equation 1, and the equivalent interfacial curvature value which is expected to manifest at each pressure was calculated using Equation 3.

## 2.4 Image acquisition and data processing

X-ray CT scans were acquired at the ANU CTLab, at 100 kV tube voltage and 65 µA target current, with 0.25 second frame acquisition rates and three frame accumulations per projection. Acquisition trajectory was a double helix, resulting in datasets with a vertical span of 7.1-7.3 mm, and the voxel resolution was 4.95, 4.90, and 4.90 µm/voxel edge for the 18, 268, and 3000 µl/hr experiments, respectively (Table 1). Helical cone-beam filtered back projection (Varslot et al., 2011) was utilized for reconstruction of the 3D tomographic data sets.

Data segmentation and post-processing was accomplished using Mango. A cylindrical subsection of radius 4.4 mm for each data series was selected for analysis. Two-phase (air and combined brine/solid) segmentation was carried out using an active contours segmentation routine (Sheppard et al., 2004). For measurement of interfacial features, the pore space occupied by wetting phase must be accurately identified, requiring precise registration of the dry sample (which is known to contain only two phases: solid and air) to the partially saturated. To facilitate a perfect registration, the drainage endpoint scan for each experiment was used as a "dry" scan for each experimental sequence, this scan was merged with the other scans to achieve three-phase (air, brine, and solid) segmentations. The drainage endpoint scans were all collected at high $P_c$ values indicating negligible residual brine saturations. Post segmentation noise removal was achieved by removing air-identified voxels which were smaller than $1.4 \times 10^{-5}$ mm$^3$, this is equivalent to a spherical pore of 15 micron radius, smaller than the smallest pore size expected for Bentheimer sandstone (Maloney et al., 1990), and voxel clusters smaller than this volume are assumed to be noise.

Visualization of (a) the raw grayscale tomographic data, and (b) the results of the processing routine are provided in Figure 2. For analysis presented in section 3.0, it is important to distinguish between nonwetting phase which is connected to the nonwetting phase reservoir above the sample, and that which is disconnected. So, for each data volume, additional data processing was conducted to separate and quantify "connected" and "disconnected" nonwetting phase, i.e. nonwetting phase which spans to the top (reaches the maximum of the z range) of the volume (black-labeled clusters in Figure 2 (b)), and that which is disconnected and isolated from the top of the data volume (red-labeled clusters in Figure 2 (b)).

## 2.5 Image-based curvature measurement

Image-based curvatures between the wetting (brine) and nonwetting (air) phases are measured using (1) the final three-phase segmented data volume of the partially-saturated sample, (2) the Euclidean distance map of the pore space (calculated from the "dry" image), and (3) the original grayscale tomogram of the partially-saturated sample. This method of curvature analysis thus requires sub-voxel precise registration between the "dry" pore-space volume and the partially-saturated volumes. In order to avoid mismeasurements due to partial volume effects and imprecise segmentation near the three-phase contact line we neglect curvature measurements near the solid surface and also more highly weight curvature measurements farther from the solid surface, following the curvature estimation method proposed by (Li et al., n.d.). The process follows the steps outlined below:

1. Using the three-phase segmented data, a list of all wetting-nonwetting interface voxel pairs is created.
2. A tomographic threshold is estimated by finding the value that most often lies between the tomographic values of interface voxel pairs.
3. Seed points are planted on all of the wetting-nonwetting interfaces identified in the three-phase segmented data.

4. Seed locations are compared to the Euclidean distance map of the pore space (calculated from the two-phase segmentation of the "dry" image), and locations which are within 20% (by distance) of the solid surface are removed from further analysis.

5. Each seed point is used to generate a cloud of up to 15 neighbouring voxel pairs. A cloud of points is then created by calculating where the tomographic threshold would linearly lie between each voxel pair. This ensures that pixilation does not influence the curvature estimate, but without using a mesh or surface generation method, as has been used previously (Andrew et al., 2015, 2014; Armstrong et al., 2012; Li et al., n.d.).

6. The points are compared to the Euclidean distance map of the pore space and are weighted according to their distance from the solid surface, giving points at the terminus of a meniscus a higher weighting.

7. The clouds of points are input into a "Monge Fitting" CGAL library routine, which outputs the two principle curvatures.

8. The mean curvature is calculated as the average of the two principle curvatures following eqn.4.

For each data volume, histograms of the mean curvature values were produced, and a curve was fit to the peak of the histogram. The peak of the fitted curve represents the mean curvature of the entire data volume. In addition to this overall curvature value, curvatures were also calculated for individual clusters: each cloud of points is associated with a specific (labeled) cluster of nonwetting phase (some labels have more than one cloud of points; for the largest cluster, up to 25,000 seeds are used); labels for each cluster are archived so that the curvature measurements can be linked to the individual volume and connectivity values for each cluster.

## 3.0 Results

### 3.1 Transducer-based Pc-S curves

Capillary pressure-saturation ($P_C$-S) curves for the three drainage experiments were constructed by pairing image-based saturation information with time-averaged transducer-based $P_C$ values (Figure 3). The total range of measured pressure is indicated by error bars in Figure 3 (the range of pressure measurement for many data points is smaller than the data symbol). The $P_C$-S curves measured here indicate an air-entry pressure <4 kPa, and a mid-saturation plateau at approx. 5-6 kPa; this is consistent with previous $P_C$-S experiments in Bentheimer sandstone (Herring et al., 2014; Raeesi et al., 2014). We note that all the curves are shifted away from 100% towards low brine saturations along the x-axis, as they all had some amount of air initially due to incomplete vacuum saturation process.

The drainage branch of the $P_C$-S curve for highest flow rate experiment (3000 µl/hr, drainage Ca of 5.3 x $10^{-8}$, see Table 1) is inconsistent with the curves for the medium flow rate (268 µl/hr, drainage Ca of 4.8 x $10^{-9}$) and slow flow rate (18 µl/hr, drainage of Ca 3.2 x $10^{-1}$) experiments. In the brine saturation region of 30-40%, the transducer-measured $P_C$ values are elevated by approximately 1.4 kPa, equivalent to an increase of approx. 25% relative to low and medium flow rate experiments (Figure 3(b)). As brine saturation decreases beyond 30%, the $P_C$-S curves for all experiments converge. We further investigate this unexpected behaviour by inspecting the curvature-based $P_C$ values in the next sections.

*3.2 Comparison between image- and transducer-based curvature measurements*

Following the discussion in section 1.0, we assume that only nonwetting phase which is connected to the nonwetting phase reservoir will exhibit (microscopic) curvature values signified by the (macroscopic) transducer-measured $P_C$ values. The match between curvature values measured from connected nonwetting – wetting phase interfaces from the images and estimated from transducer-based pressure measurements is shown in Figure 4. Although the bulk of the data demonstrates a relatively good match between image- and transducer-based values, we identify some obvious and consistent outliers.

We propose that there are two image-based factors which could result in inapplicability of image-based curvature measurements: (1) low interfacial area values, resulting in inadequate statistics for curvature calculations, and (2) high curvature values, which are affected by voxel resolution. The error (difference) between image- and transducer based curvature values as a function of these two parameters are shown in Figure 5 (a) and (b), respectively. A third source of discrepancy between the image- and transducer-based curvature measures is due to lack of equilibration at very low wetting phase saturations (i.e. very high $P_C$/curvature values). In this case the thin layers of brine within the rock sample require significant additional time to redistribute and reach equilibrium (e.g., see transient pressure response at low brine pressure in Figure 1, and saturation region where error bars become significant in Figure 3). Figure 5 (c) shows the error (difference) between image- and transducer based curvature values as a function of nonwetting phase saturation.

Via inspection of Figure 5, we identify three criteria for which image-based curvature values do not match transducer-based curvature estimates:

- Connected nonwetting-wetting interfacial area per volume values < 250 mm$^{-1}$
- Transducer-based curvature values indicating $P_C$> 6.5 kPa, equivalent to curvature values of 0.225 voxel$^{-1}$.
- Nonwetting phase saturation > 82% (i.e. wetting phase saturation < 18%)

Physically, this indicates that data collected at saturation extremes are more likely to demonstrate a mismatch between transducer- and image-based $P_C$ values. At high wetting phase saturation (low nonwetting phase saturation) just after the start of drainage, the wetting-nonwetting phase interfacial area is likely to be too small to deliver adequate statistics, as interfacial area peaks at mid-range saturation values (e.g. Culligan et al., 2004; Porter et al., 2010). At the opposite saturation extreme, the three criteria are interlinked: high nonwetting phase saturation (low wetting phase saturation) indicates high $P_C$ and low interfacial area values.

Table 2 displays the root-mean-square error (RMSE) between the image- and transducer-based curvature values for the following cases: (1) all original data, (2) data excluded based on low interfacial area per volume, (3) data excluded based on transducer-predicted high curvature, (4) data excluded based on low wetting phase saturations, and (5) data excluded based on both interfacial area and curvature criteria. For this set of experiments, the data points excluded by application of the maximum curvature criterion (case 3) contained all but one of the data points that would have been excluded based on saturation (case 4); so even though the physical reasons which underlie these two criteria are different, application of either criterion provides effectively the same result.

We note here that, by necessity, we use the transducer-based curvature estimates to provide a prediction of the image-based curvature estimate. Because the transducer-based $P_C$-S curve for the 3000 μL/hr experiment was elevated by ~1.4 kPa relative to the 18 and 268 μL/hr $P_C$-S curves at intermediate saturation range (Figure 3 (b)), almost all data points collected during the drainage process for the 3000 μL/hr experiment comprise transducer-based curvature estimates greater than 0.225 voxel$^{-1}$. In order to investigate whether the image-based curvature values supported the elevated $P_C$-S relationship indicated by transducer measurements, we included data which exceeded the (transducer-estimated) curvature criteria threshold by 1.4 kPa (i.e. we included data for which the transducer-based curvature estimates predicted curvatures of up to 0.27 voxel$^{-1}$) for the 3000 μL/hr data.

### 3.3. Connected nonwetting phase and evaluation of equilibrium condition

For the range of curvature for which our curvature algorithm is applicable (i.e. transducer measured $P_C$ < 6.5 kPa (curvature values < 0.225 voxel$^{-1}$) for 18 and 268 μl/hr experiments and $P_C$ < 7.9 kPa (curvature values < 0.27 voxel$^{-1}$) for the 3000 μl/hr experiment) the match between the image- and transducer-based curvature estimates is relatively good, resulting in RMSE values of 0.030, 0.009, and 0.043 (equivalent to 13.3%, 4.0%, and 15.9% of the maximum curvatures measured) for the 18, 268, and 3000 μl/hr flow rate experiments, respectively (Table 2). Gray et al. (2015) suggest that the match between image-based curvature values and pressure transducer measures provides an indication of whether equilibrium has been reached; the relatively good fit for 18 and 268 μl/hr flow rate experiments indicates that the equilibration periods used in these experiments are adequate for $P_C$ values < 6.5 kPa.

The equilibration condition of the highest flow rate condition (3000 μl/hr) is more difficult to determine, given the reduced goodness of fit between transducer- and image-based curvature values at curvature values near 0.20 voxel$^{-1}$ as demonstrated in Figure 6. To investigate the possibility that the interfaces in the 3000 μl/hr are out of equilibrium, representative histograms of the range and frequency of curvature values measured on the connected nonwetting-wetting phase interfaces for all three experiments are presented in Figure 7. For the data volumes presented in Figure 7, the mean curvature value as determined by curve fitting was 0.19 voxel$^{-1}$ (5.6 kPa). For a system out of equilibrium, we would expect to observe a distinct difference in distribution of curvature values present in the system; i.e. perhaps a long tail indicating elevated local $P_C$ values. Figure 7 demonstrates that the 18, 268, and 3000 μl/hr experiments display very similar range and shape of curvature distributions, suggesting that all systems represent equivalent equilibrium conditions at this particular $P_C$ condition; thus the reduced goodness of fit of the 3000 μl/hr experiments cannot be attributed to (lack of) equilibrium conditions. Additional interpretation of the reduced goodness of fit of the 3000 μl/hr data is presented in Section 3.5.

Comparison of the pressure response during scanning periods (Figure 1) and the range of pressure recorded during scanning as indicated by the error bars on the transducer-based $P_C$-S curves (Figure 3) demonstrates that significant pressure changes (as recorded by the transducer) during scanning periods occur at wetting phase saturations less than approx. 10%, and are most obvious in the 3000 μl/hr experiment. At these low saturation levels, most large pore spaces are filled with nonwetting phase and the wetting phase relative permeability is expected to be reduced by orders of magnitude relative to higher brine saturation levels, therefore requiring longer timeframes for equilibration. We emphasize that no indication of large pore-body sized fluid movements (i.e. blurring) is present in the tomographic data for any of the flow rate conditions investigated; and for all experiments, almost the entirety of the core (barring thin bands of less than 1 mm within the top and bottom edges of the core) is within the field of view of scanning. That is, the overall

distribution of fluid phases throughout the core is stable for the duration of each scan (i.e. 80-90 minutes), implying that any fluid equilibration process must be occurring on the sub-pore scale. Unfortunately, for these low brine saturation data, we cannot use the image-based data to evaluate this issue due to the image resolution limitations of the curvature algorithm.

### 3.4 Disconnected nonwetting phase

For all three flow rate conditions, disconnected clusters of air were present during both drainage and imbibition. The curvature value for each individual cluster, as well as its relative volume (as indicated by the size of each circular data symbol), are presented together on Figure 8 as a function of the overall system saturation during (a) drainage, and (b) imbibition. Given the resolution limitations of the curvature algorithm, it is unclear whether curvatures measured on very small clusters can be considered to be accurate; however, for completeness, the entirety of the curvature-volume distribution data is included in Figure 8. To provide context for these disconnected cluster values, the transducer-based $P_C$-$S$ curve for the 18 µl/hr experiment is overlaid on each plot.

Curvature values less than 0.0 indicate the presence of concave air bubbles, which are not physically possible for this water-wet sandstone; however, the results of the curvature algorithm did produce some negative curvature values for individual clusters. These curvature measurements are assumed to be errors due to image artifacts, but are included on Figure 8 for completeness and to give an indication of the occurrence of mismeasurements; as shown, the frequency of physically unrealistic (negative) curvature values is negligible.

For all flow rate conditions, the disconnected cluster curvature-size profiles measured at the initial condition (wetting phase saturation of 0.94, 0.75, and 0.95 for 18 µl/hr, 268 µl/hr, and 3000 µl/hr flow rate experiments, respectively) do not remain constant as drainage proceeds; rather, both the size and curvature distributions of the clusters broaden and evolve during drainage (Figure 8 (a)). Although some measured curvature values for disconnected clusters indicate that they exist at higher $P_C$ relative to the equivalent connected phase $P_C$, most disconnected clusters exhibit curvature values between 0 and the connected phase $P_C$; a similar pressure distribution has been reported for oil ganglia in glass bead columns (Li et al., n.d.).

For all flow rate conditions, isolated clusters exist during drainage for wetting phase saturation values greater than 10% (as air saturation increases past 90%, all air present in the sample becomes connected and spans to the top of the sample and the nonwetting phase reservoir). Notably, relatively large isolated clusters are present even at saturation levels indicating the nonwetting phase percolation threshold has been achieved (i.e. nonwetting phase saturations above approx. 50% (Herring et al., 2015)), particularly for the highest flow rate condition. These observations indicate that during quasi-static experiments, for all flow rates investigated, a significant level of snap-off occurs during drainage; this observation is supported by other quasi-static experiments (Li et al., n.d.), as well as by observations during dynamic imaging experiments which demonstrate dynamic connectivity during steady state co-current flow (Reynolds et al., 2015), and snap-off and ganglia growth during drainage (Andrew et al., 2015). Furthermore, our experiments indicate that snap-off is more prevalent as flow rate increases (Figure 8 (a)); potentially reflecting the impact of viscous and inertial forces on displacements occurring during drainage.

During early imbibition (wetting phase saturation <40%), isolated clusters are smaller and demonstrate a narrow range of relatively low curvatures compared to the connected phase pressure (Figure 8 (b)); this is contrary to other experimental observations which indicate that during imbibition, disconnected clusters maintain the pressure value at which snap-off occurred, i.e. curvatures indicating pressure greater than the connected phase pressure should be observed (Li et al., n.d.). The lack of high-curvature cluster measurements in these experiments is likely an artifact of the curvature algorithm which has been shown to be inapplicable for measurement of curvature values > 0.225 voxel$^{-1}$ (Pc >~6.5 kPa). At the end of imbibition (wetting saturation of approx. 60%), the data indicate larger isolated clusters and a wider range of curvature values (generally at greater curvature than the equivalent connected phase $P_C$) than is apparent at comparable saturation levels during drainage.

The occurrence of snap-off events observed in these experiments, while observed in other quasi-static and dynamic experiments, could be enhanced by the compressibility of the nonwetting fluid (ambient condition air), or by the quasi-static nature of the observations. Comparison with experiments using an incompressible nonwetting phase, and with dynamic imaging methods, is necessary to determine the applicability of the cluster distributions measured here (in terms of frequency, $P_C$, and volume) for other systems.

*3.5 Inconsistencies in $P_C$ measurements at high flow rate conditions*

The data collected from the 3000 μl/hr experiment is inconsistent with that collected from the 18 and 268 μl/hr experiments in two important aspects: (a) the pattern of transducer-measured $P_C$ during drainage which shows elevated $P_C$ at intermediate $S_w$ ranges, followed by $P_C$ values which converge to the curves measured for lower flow rates as $S_w$ decreases beyond 30% (Figure 3 (b)); and (b) the relatively poor fit between transducer- and image-based curvature estimates with transducer-based estimates being consistently higher than image-based curvature estimates (Figure 6).

We propose the following explanation to account for these discrepancies:

Upon initiation of pumping, the very high flow rate used in the 3000 μl/hr experiment results in the establishment of high and sharp $P_C$ boundary conditions at the bottom of the core. This produces a distinctly different distribution of fluid flow compared to the lower flow rate experiments; rather than flow which is dominated by invasion percolation, the high flow rate/high $P_C$ quickly forces nonwetting phase into very small pore spaces. This process is likely enhanced near the hydrophilic membrane which is compressed to the base of the core; however, during these experiments the membrane itself was not included in the imaged section of the core. These accelerated displacement processes (which may include a combination of local pore emptying and refilling events) and the accompanying high occurrence of snap-off events in this experiment (Figure 8) act to stabilize the wetting phase in a high $P_C$ configuration, particularly at the lower boundary of the core adjacent to the membrane. Thus, while the $P_C$ measured via transducer (which only measures connected brine phase, recall the nonwetting phase is assumed to exist at ambient pressure) reflects a relatively high $P_C$, the local curvatures measured on the interfaces between the brine phase and air phases reflect a lower $P_C$. As drainage continues and brine saturation decreases below 30%, the previously "snapped-off" air clusters become reconnected to the bulk air phase, and the stabilizing impact of these disconnected clusters lessens, which results in the gradual convergence of the 3000 μl/hr $P_C$-S curve to the 18 and 268 μl/hr $P_C$-S curves. During imbibition, the nonwetting phase remains more highly connected with the bulk phase until snap-off occurs (Herring et al., 2013; Schlüter et al., 2016), so the air clusters which are disconnected during imbibition

retain pressure values equivalent to the ambient bulk phase pressure, and $P_C$-S data measured during this process (while limited in number) are not offset from the data measured for the slower flow rates (Figure 6).

## 4.0 Summary

We present results from a series of quasi-static drainage-imbibition experiments with air (nonwetting phase) and brine (wetting phase) in Bentheimer sandstone cores, where flow rates ranged three orders of magnitude. We pair bulk-phase $P_C$ values, measured over the core via transducer, with quantitative x-ray tomographic image-based information. We compare the transducer-based $P_C$ to 3D image-based curvature values, calculated with a novel algorithm which utilizes a combination of segmented and grayscale tomographic images to measure the wetting-nonwetting interface curvature. We find that our curvature algorithm is consistent with transducer-based pressure values (and thus applicable for measurement) for the range of curvature between 0 and approx. 0.225 voxel$^{-1}$; for this data set, this corresponds to $P_C$ values of 0 to approx. 6.5 kPa and a minimum radius of curvature of approx. 20 µm; this represents a significant increase in the maximum $P_C$ and the minimum radius of curvature which has been successfully measured from 3D tomographic images previously.

Although the transient pressure response indicates dramatic differences in $P_C$ for the different flow rate experiments, the equilibrium quasi-static curvature values (both transducer- and image-based) demonstrate that the baseline $P_C$-S curve is replicated under a wide range of flow rate conditions; and that for values between 0 and 6.5 kPa, the brine-air-sandstone system as imaged represents equilibrium conditions. For scans acquired at $P_C$ greater than 6.5 kPa (approximately equivalent to brine saturation <18%), the transducer-measured pressure values display transient pressure responses, signifying that longer equilibration periods are required for these conditions.

During drainage, we observe evidence of snap-off of relatively large (>> one pore body) air clusters for all three flow rate conditions. Relatively large volume snap-off events persist at high air saturation levels (even above the air percolation threshold), and are more likely to persist at higher air saturation as flow rate increases. Snap-off which occurs during imbibition results in a final curvature-volume distribution of disconnected clusters which is wider and more heterogeneous than that observed at similar saturation levels for drainage.

The experiment conducted at the highest flow rate condition of 3000 µl/hr displays inconsistent $P_C$-S behavior relative to the slower flow rate conditions, and also demonstrates a relatively poor fit between transducer- and image-based curvature estimates. We propose that these observations are the result of high flow rate imposing sharp $P_C$ boundary conditions which dictate a distribution of fluids near the bottom of the core reflective of a high $P_C$, which are stabilized due to high rates of snap-off during the drainage process. Throughout the rest of the core, interfaces between connected nonwetting phase and wetting phase indicate lower $P_C$ values (more similar to the slow flow rate experiments). The causes and effects of snap-off during drainage require more investigation to determine the relevance and ramifications for multiphase flow theory and processes.

References

Andrew, M., Bijeljic, B., Blunt, M.J., 2014. Pore-by-pore capillary pressure measurements using X-ray microtomography at reservoir conditions: Curvature, snap-off, and remobilization of residual CO 2. Water Resour. Res. 50, 8760–8774. doi:10.1002/2014WR015970

Andrew, M., Menke, H., Blunt, M.J., Bijeljic, B., 2015. The Imaging of Dynamic Multiphase Fluid Flow Using Synchrotron-Based X-ray Microtomography at Reservoir Conditions. Transp. Porous Media 110, 1–24. doi:10.1007/s11242-015-0553-2

Armstrong, R.T., Georgiadis, A., Ott, H., Klemin, D., Berg, S., 2014. Critical capillary number: Desaturation studied with fast X-ray computed microtomography. Geophys. Res. Lett. 41, 55–60.

Armstrong, R.T., Porter, M.L., Wildenschild, D., 2012. Linking pore-scale interfacial curvature to column-scale capillary pressure. Adv. Water Resour. 46, 55–62. doi:10.1016/j.advwatres.2012.05.009

Avraam, D.G., Payatakes, A.C., 1995. Flow regimes and relative permeabilities during steady-state two-phase flow in porous media. J. Fluid Mech. 293, 207. doi:10.1017/S0022112095001698

Bear, J., 1972. Dynamics of fluids in porous materials.

Berg, S., Ott, H., Klapp, S.A., Schwing, A., Neiteler, R., Brussee, N., Makurat, A., Leu, L., Enzmann, F., Schwarz, J.-O., Kersten, M., Irvine, S., Stampanoni, M., 2013. Real-time 3D imaging of Haines jumps in porous media flow. Proc. Natl. Acad. Sci. U. S. A. 110, 5.

Besserer, H., Hilfer, R., 2000. Old problems and new solutions for multiphase flow in porous media. Porous Media Physics, Model. Simul.

Culligan, K.A., Wildenschild, D., Christensen, B.S.B., Gray, W.G., Rivers, M.L., 2006. Pore-scale characteristics of multiphase flow in porous media: a comparison of air–water and oil–water experiments. Adv. Water Resour. 29, 227–238.

Culligan, K.A., Wildenschild, D., Christensen, B.S.B., Gray, W.G., Rivers, M.L., Tompson, A.F.B., 2004. Interfacial area measurements for unsaturated flow through a porous medium. Water Resour. Res 40, W12413.

Fischer, U., Dury, O., Fliihler, H., Th van Genuchten, M., 1997. Modeling Nonwetting-Phase Relative Permeability Accounting for a Discontinuous

Nonwetting Phase.

Gray, W.G., Dye, A.L., McClure, J.E., Pyrak-Nolte, L.J., Miller, C.T., 2015. On the dynamics and kinematics of two-fluid-phase flow in porous media. Water Resour. Res. 51, 5365–5381. doi:10.1002/2015WR016921

Haines, W.B., 1927. Studies in the physical properties of soils: IV. A further contribution to the theory of capillary phenomena in soil. J. Agric. Sci. 17, 264–290. doi:10.1017/S0021859600018499

Hassanizadeh, S.M., Gray, W.G., 1993. Thermodynamic basis of capillary pressure in porous media. Water Resour. Res. 29, 3389–3405. doi:10.1029/93wr01495

Herring, A.L., Andersson, L., Newell, D., Carey, J.W., Wildenschild, D., 2014. Pore-scale observations of supercritical CO2 drainage in Bentheimer sandstone by synchrotron x-ray imaging. Int. J. Greenh. Gas Control 25, 93–101. doi:10.1016/j.ijggc.2014.04.003

Herring, A.L., Andersson, L., Schlüter, S., Sheppard, A., Wildenschild, D., 2015. Efficiently Engineering Pore-Scale Processes: Force Balance and Topology During Nonwetting Phase Trapping in Porous Media. Adv. Water Resour. 79, 91–102. doi:10.1016/j.advwatres.2015.02.005

Herring, A.L., Andersson, L., Wildenschild, D., 2016a. Enhancing residual trapping of supercritical CO2 via cyclic injections. Geophys. Res. Lett. doi:10.1002/2016GL070304

Herring, A.L., Harper, E.J., Andersson, L., Sheppard, A., Bay, B.K., Wildenschild, D., 2013. Effect of fluid topology on residual nonwetting phase trapping: Implications for geologic CO2 sequestration. Adv. Water Resour. 62, 47–58. doi:10.1016/j.advwatres.2013.09.015

Herring, A.L., Sheppard, A., Andersson, L., Wildenschild, D., 2016b. Impact of wettability alteration on 3D nonwetting phase trapping and transport. Int. J. Greenh. Gas Control 46, 175–186. doi:10.1016/j.ijggc.2015.12.026

Hilfer, R., 2006. Macroscopic capillarity and hysteresis for flow in porous media. Phys. Rev. E 73, 16307. doi:10.1103/PhysRevE.73.016307

Hilfer, R., 1998. Macroscopic equations of motion for two-phase flow in porous media. Phys. Rev. E 58, 2090–2096. doi:10.1103/PhysRevE.58.2090

Hilfer, R., Armstrong, R.T., Berg, S., Georgiadis, A., Ott, H., 2015. Capillary saturation and desaturation. Phys. Rev. E 92, 63023. doi:10.1103/PhysRevE.92.063023

Hilfer, R., Doster, F., 2010. Percolation as a Basic Concept for Macroscopic Capillarity. Transp Porous Med 82, 507–519. doi:10.1007/s11242-009-9395-0

Hou, L., Chen, L., Kibbey, T.C.G., 2012. Dynamic capillary effects in a small-volume unsaturated porous medium: Implications of sensor response and gas pressure gradients for understanding system dependencies. Water Resour. Res. 48, n/a-n/a. doi:10.1029/2012WR012434

Li, T., Dragila, M.I., Wildenschild, D., n.d. An Improved Method for Estimating Capillary Pressure from 3D Microtomography Images and its Application to the

Study of Disconnected Nonwetting Phase.

Maloney, D.R., Honarpour, M.M., Brinkmeyer, A.D., 1990. The effects of rock characteristics on relative permeability.

Morrow, N.R., 1990. Wettability and its effect on oil recovery. J. Pet. Technol. 24:12.

Peksa, A.E., Wolf, K.-H.A.A., Slob, E.C., Chmura, Ł., Zitha, P.L.J., 2016. Original and pyrometamorphical altered Bentheimer sandstone; petrophysical properties, surface and dielectric behavior. J. Pet. Sci. Eng. doi:10.1016/j.petrol.2016.10.024

Peksa, A.E., Wolf, K.-H.A.A., Zitha, P.L.J., 2015. Bentheimer sandstone revisited for experimental purposes. Mar. Pet. Geol. 67, 701–719. doi:10.1016/j.marpetgeo.2015.06.001

Plug, W.J., Bruining, J., 2007. Capillary pressure for the sand-CO2-water system under various pressure conditions. Application to CO2 sequestration. Adv. Water Resour. 30, 2339–2353. doi:10.1016/j.advwatres.2007.05.010

Porter, M.L., Wildenschild, D., Grant, G., Gerhard, J.I., 2010. Measurement and prediction of the relationship between capillary pressure, saturation, and interfacial area in a NAPL-water-glass bead system. Water Resour. Res. 46, n/a-n/a. doi:10.1029/2009WR007786

Raeesi, B., Morrow, N.R., Mason, G., 2014. Capillary Pressure Hysteresis Behavior of Three Sandstones Measured with a Multistep Outflow–Inflow Apparatus. Vadose Zo. J. 13. doi:10.2136/vzj2013.06.0097

Reynolds, C., Menke, H., Blunt, M., Krevor, S., 2015. Observations of the Dynamic Connectivity of the Non-Wetting Phase During Steady State Flow at the Pore Scale Using 3D X-ray Microtomography, in: American Geophysical Union Fall Meeting. San Francisco, CA.

Rücker, M., Berg, S., Armstrong, R.T., Georgiadis, A., Ott, H., Schwing, A., Neiteler, R., Brussee, N., Makurat, A., Leu, L., Wolf, M., Khan, F., Enzmann, F., Kersten, M., 2015. From connected pathway flow to ganglion dynamics. Geophys. Res. Lett. doi:10.1002/2015GL064007

Schlüter, S., Berg, S., Rücker, M., Armstrong, R.T., Vogel, H.-J., Hilfer, R., Wildenschild, D., 2016. Pore-scale displacement mechanisms as a source of hysteresis for two-phase flow in porous media. Water Resour. Res. 52, n/a-n/a. doi:10.1002/2015WR018254

Schlüter, S., Li, T., Vogel, H.-J., Berg, S., Wildenschild, D., n.d. Time scales of relaxation dynamics during hydraulic non-equilibrium in two-phase flow. Submitt. to Water Resour. Res.

Selker, J.S., McCord, J.T., Keller, C.K., 1999. Vadose zone processes. CRC Press.

Sheppard, A.P., Sok, R.M., Averdunk, H., 2004. Techniques for image enhancement and segmentation of tomographic images of porous materials. Phys. A Stat. Mech. its Appl. 339, 145–151. doi:10.1016/j.physa.2004.03.057

Varslot, T., Kingston, A., Myers, G., Sheppard, A., 2011. High-resolution helical cone-beam micro-CT with theoretically-exact reconstruction from

experimental data. Med. Phys. 38, 5459. doi:10.1118/1.3633900

Wildenschild, D., Hopmans, J.W., Rivers, M.L., Kent, A.J.R., 2005. Quantitative analysis of flow processes in a sand using synchrotron-based X-ray microtomography. Vadose Zo. J. 4, 112–126.

Youssef, S., Bauer, D., Bekri, S., Rosenberg, E., Vizika-kavvadias, O., 2010. 3D In-Situ Fluid Distribution Imaging at the Pore Scale as a New Tool For Multiphase Flow Studies, in: SPE Annual Technical Conference and Exhibition.
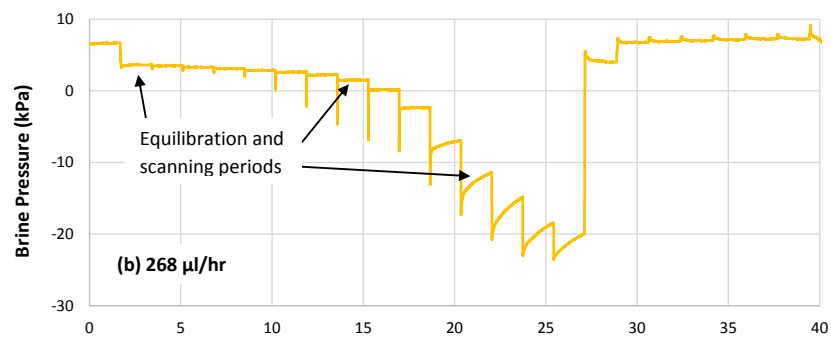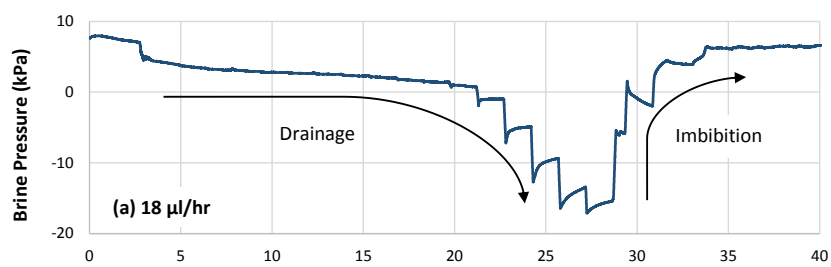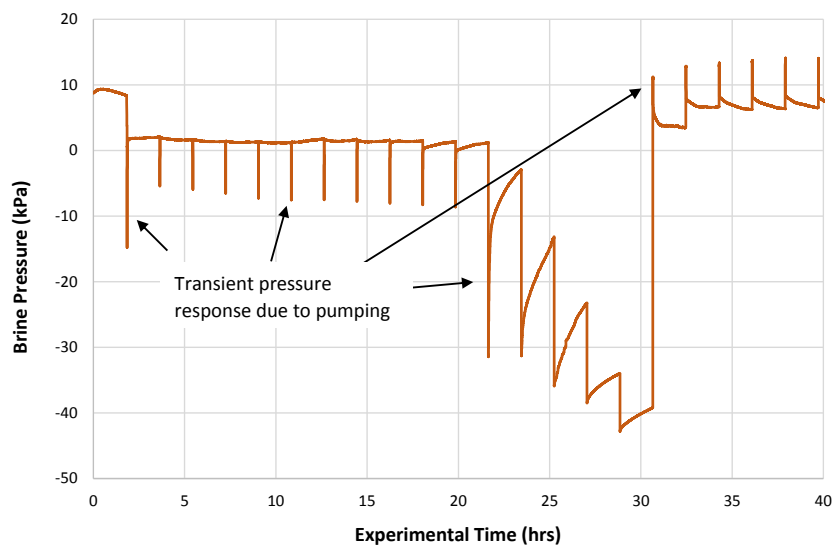
*Figure 1.* *Raw brine pressure data collected via pressure transducer for drainage-imbibition experiments conducted at three different flow rates: (a) 18 µl/hr, (b) 268 µl/hr, and (c) 3000 µl/hr. Examples of pressure response during pumping periods, as well as equilibration and scanning periods, are highlighted*

**(a)**                                          **(b)**
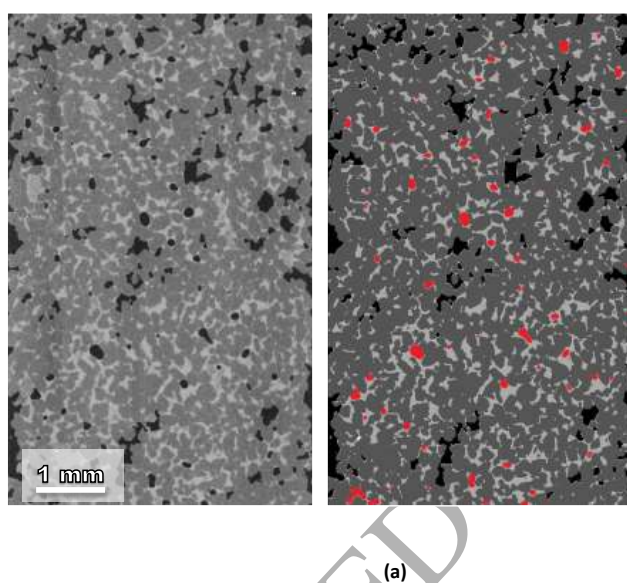
*Figure 2*. *An orthogonal slice through the vertical dimension of one volume of 3D data: (a) raw, unmodified grayscale tomographic data; and (b) the segmented representation of the data upon which quantitative metrics are measured. In (a) the brightness of the pixels reflects the x-ray attenuation of the fluid and solid phases; in (b), pixels are labeled as one of four phases: light gray signifies wetting phase (brine), dark gray indicates solid grains, connected nonwetting phase (air) which spans to the top of the core is labeled in black, and disconnected air clusters are labeled with red.*
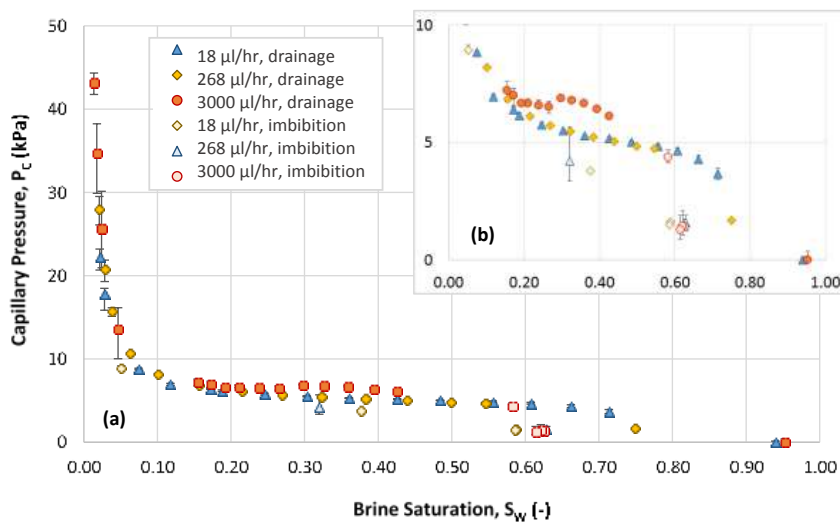
**Figure 3.** *Capillary pressure-saturation ($P_C$–S) relationships derived from average transducer-based $P_C$ values paired with wetting phase (brine) saturation ($S_W$) values measured from x-ray tomographic images for the three quasi-static drainage-imbibition experiments. The vertical error bars indicate the range of pressure measured during each specific scan (bars are smaller than the data symbol for many data points). All data are shown on (a); inset (b) shows a zoomed-in subsection for $P_C$ values between 0 and 10 kPa.*
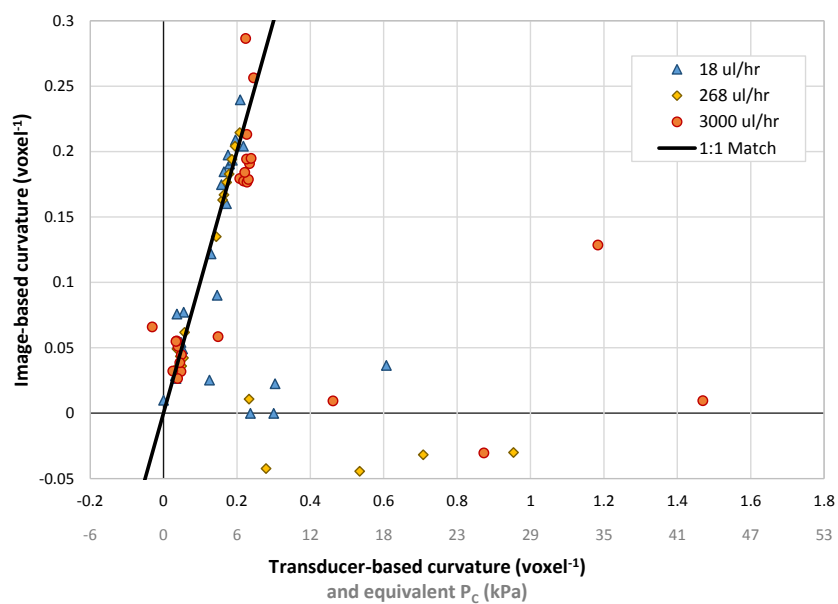
**Figure 4.** *Match between curvatures measured from x-ray tomographic images of the connected nonwetting phase, and curvatures estimated from transducer-based capillary pressure ($P_C$) measurements. $P_C$ values are indicated below the equivalent curvature values.*
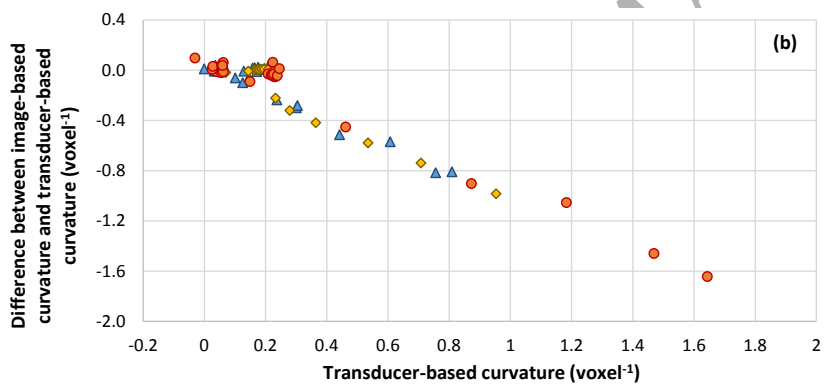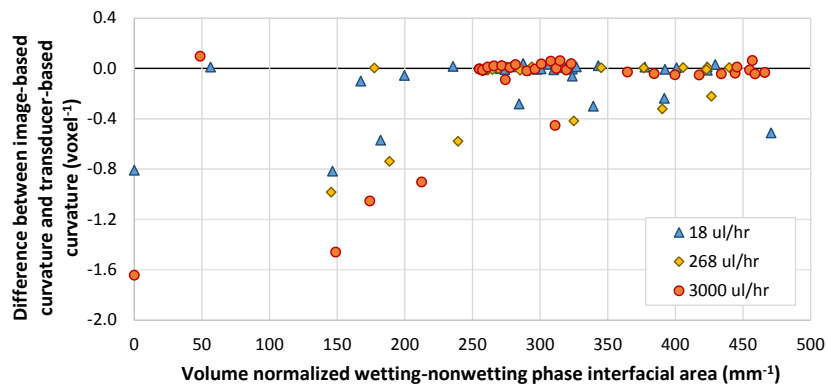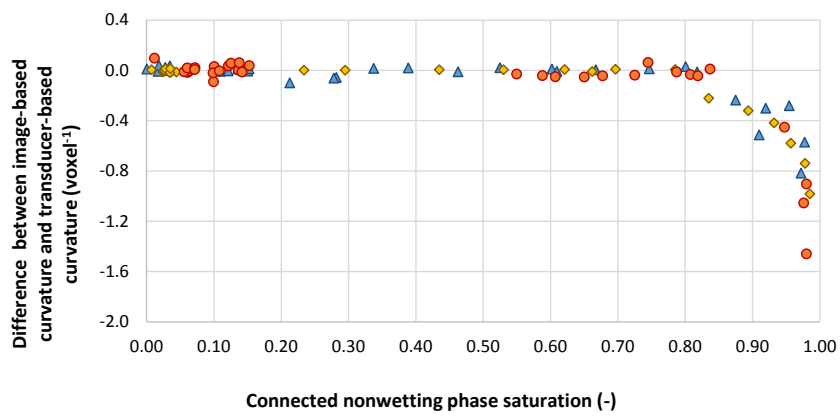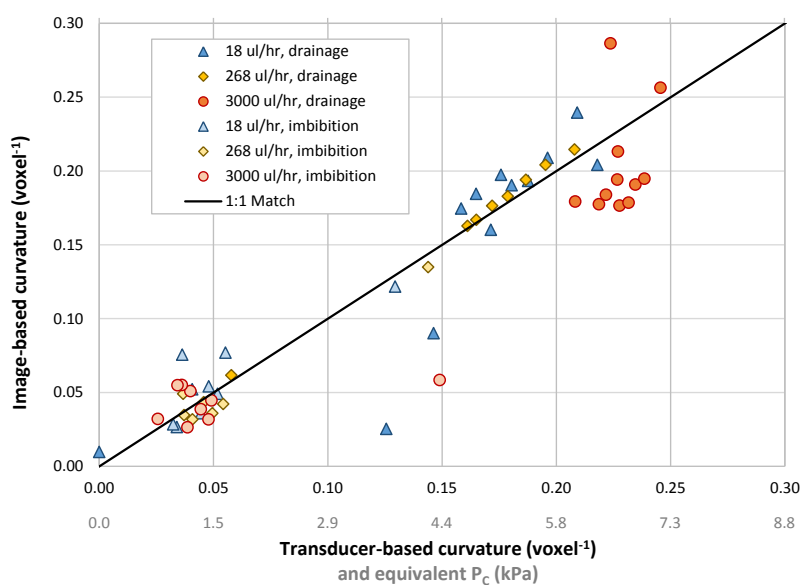
*Figure 5.* The difference between image-and transducer-based curvature estimates as a function of (a) wetting-nonwetting phase interfacial area, (b) transducer-based curvature estimates, and (c) connected nonwetting phase (air) saturation.

**(c)**

*Figure 6.* Match between curvatures measured from x-ray tomographic images of the connected nonwetting phase, and curvatures estimated from transducer-based capillary pressure ($P_C$) measurements, for data for which the transducer-based curvature value is less than 0.225 voxel$^{-1}$ (6.5 kPa) for 18 and 268 μl/hr experiments, and 0.27 voxel$^{-1}$ (7.9 kPa) for the 3000 μl/hr experiments. $P_C$ values are indicated below the equivalent curvature values.

Figure 7. Normalized histograms of the curvature values measured on connected nonwetting-wetting phase interfaces for 18, 268, and 3000 µl/hr experiments. For these specific data volumes, the curvature as determined by curve fitting was determined to be 0.19 voxel-1 (indicated by the bold vertical line). Bin size for each histogram was 0.01 voxel-1.
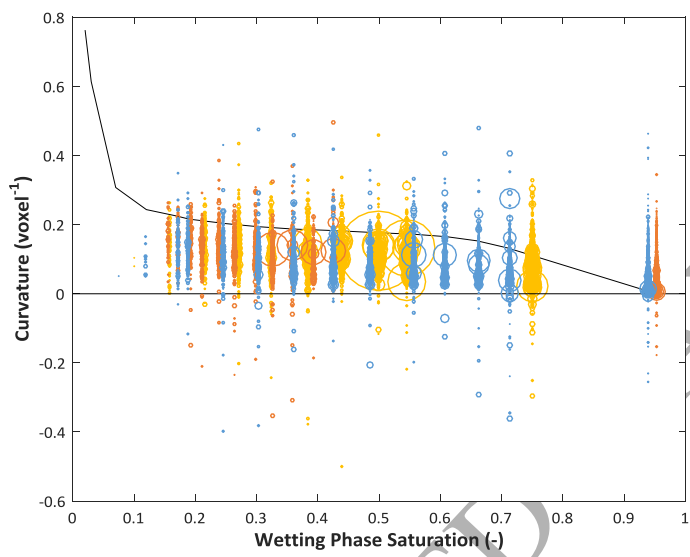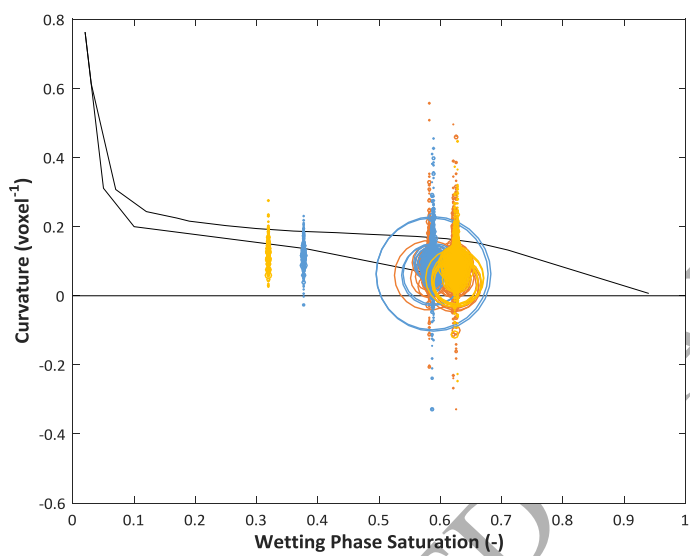
**Figure 8.** Curvature-volume distributions for disconnected nonwetting phase (air) ganglia as a function of the overall wetting phase saturation for (a) drainage and (b) imbibition. The relative volume of each ganglia is indicated by the size of each circular data point. The transducer-based capillary pressure-saturation ($P_C$-$S$) curves for the 18 µl/hr experiment are also plotted for clarity.

*Table 1.* Experimental and data processing parameters for the three drainage-imbibition experiments.

| Drainage and Imbibition Flow Rate | Drainage Ca* | Imbibition Ca* | Physical size of analyzed data | | Voxel resolution of data (μm/ voxel edge) |
|---|---|---|---|---|---|
| | | | Diameter (mm) | Height (mm) | |
| 18 μl/hr | $3.2 \times 10^{-10}$ | $2.0 \times 10^{-8}$ | 4.4 | 7.1 | 4.95 |
| 268 μl/hr | $4.8 \times 10^{-9}$ | $3.0 \times 10^{-7}$ | 4.4 | 7.3 | 4.90 |
| 3000 μl/hr | $5.3 \times 10^{-8}$ | $3.3 \times 10^{-6}$ | 4.4 | 7.3 | 4.90 |

*Calculated as Ca = μv/σ, where μ is the viscosity of the invading phase; v is the velocity of the invading phase; and σ is the interfacial tension between the two fluid phases.

**Table 2.** *Statistical analysis of the match between image- and transducer-based curvature estimates*

| | | Root-Mean-Square Error (number of data points, n, in parens) | | |
|---|---|---|---|---|
| | | 18 µl/hr | 268 µl/hr | 3000 µl/hr |
| (1) | All data included | 0.278 (28) | 0.315 (22) | 0.519 (26) |
| (2) | Data excluded where interfacial area/volume < 250 mm$^{-1}$ | 0.155 (21) | 0.128 (17) | 0.105 (21) |
| (3) | Data excluded where transducer data predicts curvature values > 0.225 voxel$^{-1}$ (0.27 voxel$^{-1}$ for 3000 ul/hr data) | 0.030 (21) | 0.009 (15) | 0.044 (21) |
| (4) | Data excluded where wetting phase saturation < 18% | 0.030 (21) | 0.009 (15) | 0.043 (20) |
| (5) | Data excluded where interfacial area/volume< 250 mm$^{-1}$, and transducer data predicts curvature > 0.225 voxel$^{-1}$ | 0.016 (17) | 0.008 (14) | 0.037 (20) |